JOURNAL OF SPACECRAFT AND ROCKETS
Vol. 33, No. 5, September–October 1996

Computational Study of Supersonic Lateral Jet Flow Interactions

N. Qin*
Cranfield University, Cranfield, Bedfordshire MK43 0AL, England, United Kingdom
and
G. W. Foster†
Defence Research Agency, Bedford MK41 6AE, England, United Kingdom

To gain an insight into the complex flow structure near a supersonic lateral jet in a supersonic cross flow, a computational simulation was carried out using a high-resolution Navier–Stokes solver capable of resolving both shock waves and shear layers. A novel treatment of the jet boundary conditions is presented by solving the jet nozzle problem using an isentropic theory. Results are presented for the wind-tunnel test cases performed by ONERA, and comparisons are made between the numerical simulation and the experimental measurement. Major features of the complicated interaction attributable to the combined effects of the jet and the angle of attack are simulated in the computation. Multiple vortical flow structures are observed near the jet exit, which interact with the vortical flow on the leeward side of the body at relative higher angles of attack.

Nomenclature

A	= nozzle cross area
D	= nozzle diameter
d	= distance on nozzle axis from throat to exit
$\boldsymbol{E}, \boldsymbol{F}, \boldsymbol{G}$	= Cartesian fluxes
E_t	= total energy
$\boldsymbol{H}$	= flux tensor
$\boldsymbol{i}, \boldsymbol{j}, \boldsymbol{k}$	= Cartesian unit vectors
M	= Mach number
$\boldsymbol{n}$	= surface unit normal
p	= pressure
$\boldsymbol{Q}$	= conservative variable vector in Eq. (1)
$\boldsymbol{q}$	= heat transfer vector
S	= surface
$\boldsymbol{S}$	= surface vector
T	= temperature
t	= time
u, v, w	= Cartesian velocity components
V	= volume
x, y	= coordinates in the crossflow plane
z	= coordinate in the body axis direction
z_0	= z coordinate of intersection point of nozzle axis and body surface
β	= angle between nozzle axis and body axis
ρ	= density
τ	= stress tensor
Φ	= diameter of cylindrical body
ϕ	= nozzle half-cone angle

Subscripts

i, j, k	= indices in three transformed computational coordinates
j	= jet boundary condition
t	= reservoir or total values
∞	= freestream condition

Superscripts

i	= inviscid
v	= viscous
$*$	= critical values at nozzle throat

Presented as Paper 95-2151 at the AIAA 26th Fluid Dynamics Conference, San Diego, CA, June 19–22, 1995; received July 31, 1995; revision received April 20, 1996; accepted for publication May 3, 1996.

*Lecturer, Department of Aerospace Science, College of Aeronautics. Member AIAA.

†Principal Scientific Officer, High Speed and Weapon Aerodynamics Department.

Introduction

THE ejection of a supersonic lateral jet into a supersonic external crossflow results in a highly complex flowfield leading to both local and downstream interactions. The local interactions are related to the jet obstacle effect which, at supersonic speeds, produces a detached shock and a separation of the boundary layer upstream of the nozzle. The distribution of the pressure around the nozzle, for a nozzle located on a wingless fuselage and near the center of gravity, produces a low resulting force that is generally opposed to the thrust of the nozzle (unfavorable interaction) and a slight nose-up moment in the maneuver direction. The downstream interactions are attributable to the highly vortical character of the flow downstream of the jet. The velocity induced by these vortical structures affects the lifting surfaces placed downstream, generally producing a loss of lift and moments.

Numerical simulations of such a complicated flow problem require high-order mathematical modeling involving the solution of the Navier–Stokes equations. Until recently, very few numerical simulations have been carried out to analyze this fundamental aerodynamic phenomenon. The first computational and experimental side-by-side study of a lateral jet in hypersonic flow was conducted by Shang et al.[1] using a central-differencing MacCormack-type method to solve the Navier–Stokes equations closed by the Baldwin–Lomax turbulence model. Rizzetta[2] studied numerically the problem of a two-dimensional slot injection at the surface of a flat plate into a turbulent supersonic stream. Various aspects in the κ–ε two-equation turbulence model were investigated including a low Reynolds number correction and a compressibility correction to the original model. Discrepancies between the computational results and the experimental data were attributed to the three-dimensional effects in the experiments. More recently, Dash et al.[3] computed the aerodynamic interactions attributable to lateral jets in subsonic and supersonic flows using the PARCH code. Predictions have been performed simulating experiments at ONERA for jets issuing from ogive/cylinders at various flight conditions. A thin-layer Navier–Stokes solver was adopted in the numerical simulation using either Beam–Warming central differencing or Roe's approximate Riemann solver in the discretization. For turbulence

modeling, a k–ε model has been incorporated. A rectangular nozzle exit geometry and constant flow conditions were employed at the jet exit.

A three-dimensional high-resolution finite volume Navier–Stokes solver was developed based on Osher's approximate Riemann solver,[4] which has demonstrated its capabilities in accurately simulating shock waves and shear layers.[5] This property is very desirable for the study of complicated flow problems involving shock/viscous effects interactions such as the supersonic jet-interaction problem. To gain further insight into the complicated shock/vortex structure, the high-resolution Navier–Stokes solver has been used in this study of the flow interactions near and downstream from the supersonic lateral jet. Because of the availability of extensive experimental data from ONERA on such a problem, the ONERA test cases have been chosen for the present study of supersonic jet flows.

For a detailed study of the local interaction at the jet exit, a proper jet boundary condition has to be employed. A novel jet boundary condition, based on an isentropic approximation for the flow inside the nozzle that generates the supersonic jet is introduced. A flowfield comparison was made between the computational results and the experimental data, which reveals the main features of the interaction.

High-Resolution Navier–Stokes Solution

Navier–Stokes Equations

In the finite volume formulation, the Navier–Stokes equations in their integral form are preferred to their partial differential counterparts. The law of conservation of mass, momentum, and energy over a volume V bounded by a surface S can be expressed in an integral form as

$$\frac{\partial}{\partial t}\int_V \boldsymbol{Q}\,\mathrm{d}V + \int_S (\boldsymbol{H}\cdot\boldsymbol{n})dS = 0 \tag{1}$$

which, for steady flows, reduces to

$$\int_S (\boldsymbol{H}\cdot\boldsymbol{n})dS = 0 \tag{2}$$

The flux tensor H can be written in terms of the Cartesian fluxes as

$$\boldsymbol{H} = (\boldsymbol{E}^i - \boldsymbol{E}^v)\boldsymbol{i} + (\boldsymbol{F}^i - \boldsymbol{F}^v)\boldsymbol{j} + (\boldsymbol{G}^i - \boldsymbol{G}^v)\boldsymbol{k} \tag{3}$$

$$\boldsymbol{Q} = \begin{pmatrix} \rho \\ \rho u \\ \rho v \\ \rho w \\ E_t \end{pmatrix} \quad \boldsymbol{E}^i = \begin{pmatrix} \rho u \\ \rho u^2 + p \\ \rho uv \\ \rho uw \\ (E_t + p)u \end{pmatrix} \quad \boldsymbol{F}^i = \begin{pmatrix} \rho v \\ \rho uv \\ \rho v^2 + p \\ \rho vw \\ (E_t + p)v \end{pmatrix}$$

$$\boldsymbol{G}^i = \begin{pmatrix} \rho w \\ \rho uw \\ \rho vw \\ \rho w^2 \\ (E_t + p)w \end{pmatrix} \quad \boldsymbol{E}^v = \begin{pmatrix} 0 \\ \tau_{xx} \\ \tau_{xy} \\ \tau_{xz} \\ u\tau_{xx} + v\tau_{xy} + w\tau_{xz} - q_x \end{pmatrix} \tag{4}$$

$$\boldsymbol{F}^v = \begin{pmatrix} 0 \\ \tau_{xy} \\ \tau_{yy} \\ \tau_{yz} \\ u\tau_{xy} + v\tau_{yy} + w\tau_{yz} - q_y \end{pmatrix}$$

$$\boldsymbol{G}^v = \begin{pmatrix} 0 \\ \tau_{xy} \\ \tau_{yz} \\ \tau_{zz} \\ u\tau_{xy} + v\tau_{yz} + w\tau_{zz} - q_z \end{pmatrix}$$

The molecular viscosity is calculated from the Sutherland formula.

Turbulence Modeling

For jet interaction problems, higher-order turbulence modeling is desirable and many investigators[2,3] prefer the k–ε two-equation models to algebraic models. The difficulty for the turbulence modeling is that both the near-wall turbulence and the jet-wake free shear turbulence are important in the jet interaction problem. The former is critical in the shock/boundary-layer interaction around the jet exit, whereas the latter will influence the downstream interaction. Although it is believed that higher-order turbulence models should produce better numerical results, Clark and Chan[6] and Dhinagaran and Bose[7] independently reported their findings that the Baldwin–Lomax algebraic model performed as well as or better than the two-equation models with low Reynolds number and compressibility corrections in their numerical study of the two-dimensional slot jet interaction cases investigated by Rizzetta.[2]

In the present numerical simulations, the Baldwin–Lomax algebraic model[8] with the Degani–Schiff[9] modification is used to calculate the eddy viscosity. It is more accurate for vortical flows around slender bodies than the original Baldwin–Lomax model.[10] The modification was employed for the present problem because there exist strong vortical flows both around the jet stream and on the leeward side of the body at medium to high angles of attack.

Finite Volume Discretization

Equations (1) and (2) are simple expressions of the conservation laws and are valid for each local discretized finite volume cell as well as for the global control volume. In the present finite volume discretization, the region of interest is divided into hexahedral cells denoted by (i, j, k). Applying the conservation laws [Eq. (1)] to cell (i, j, k) and assuming that the tensor $\boldsymbol{H}$ remains constant across each face of the cell and that the cell-face-area vectors are oriented in the positive coordinate directions, Eq. (1) can be written as

$$\begin{aligned}\frac{\partial}{\partial t}(V_{i,j,k}\boldsymbol{Q}_{i,j,k}) &+ \boldsymbol{H}_{i+\frac{1}{2},j,k}\cdot d\boldsymbol{S}_{i+\frac{1}{2},j,k} - \boldsymbol{H}_{i-\frac{1}{2},j,k}\cdot d\boldsymbol{S}_{i-\frac{1}{2},j,k} \\ &+ \boldsymbol{H}_{i,j+\frac{1}{2},k}\cdot d\boldsymbol{S}_{i,j+\frac{1}{2},k} - \boldsymbol{H}_{i,j-\frac{1}{2},k}\cdot d\boldsymbol{S}_{i,j-\frac{1}{2},k} \\ &+ \boldsymbol{H}_{i,j,k+\frac{1}{2}}\cdot d\boldsymbol{S}_{i,j,k+\frac{1}{2}} - \boldsymbol{H}_{i,j,k-\frac{1}{2}}\cdot d\boldsymbol{S}_{i,j,k-\frac{1}{2}} = 0\end{aligned} \tag{5}$$

Each cell face may be considered to consist of two planar triangles so that the cell-face surface-area vector $d\boldsymbol{S}$ is provided by summing the triangle area vectors, which is independent on the choice of the cell-face diagonal lines. Unlike the surface areas, the cell volume is dependent on the manner in which the cell faces are broken up. Therefore, the volume calculation has to be consistent for the neighboring cells so that the sum of all the cell volumes equals the total volume of the region.

Osher's High-Resolution Solver

The numerical integration scheme produces volume-average flow properties, which are assigned to the locations of the centers of the hexahedral cells. An algorithm is to be determined for the evaluation of the flux vectors at the interfaces, which combines two distinct sets of state quantities, representing the states on both sides of the interface, into one set of fluxes normal to the interfaces. The conservation laws in Eq. (5) also can be written as

$$\begin{aligned}\frac{\partial}{\partial t}(V_{i,j,k}\boldsymbol{Q}_{i,j,k}) &+ \tilde{\boldsymbol{E}}_{i+\frac{1}{2},j,k} - \tilde{\boldsymbol{E}}_{i-\frac{1}{2},j,k} \\ &+ \tilde{\boldsymbol{F}}_{i,j+\frac{1}{2},k} - \tilde{\boldsymbol{F}}_{i,j-\frac{1}{2},k} + \tilde{\boldsymbol{G}}_{i,j,k+\frac{1}{2}} - \tilde{\boldsymbol{G}}_{i,j,k-\frac{1}{2}} = 0\end{aligned} \tag{6}$$

To account for the inviscid interaction of the adjacent fluid cells at their interface, a local wave system is solved using the approximate Riemann solver based on Osher's scheme. It leads to the flux formula for the convective term as

$$\begin{aligned}\tilde{\boldsymbol{E}}_{i+\frac{1}{2},j,k} &= \frac{1}{2}\left[\tilde{\boldsymbol{E}}\left(\boldsymbol{Q}^-, d\boldsymbol{S}_{i+\frac{1}{2},j,k}\right) + \tilde{\boldsymbol{E}}\left(\boldsymbol{Q}^+, d\boldsymbol{S}_{i+\frac{1}{2},j,k}\right)\right] \\ &- \frac{1}{2}\int_{Q^-}^{Q^+}\left|\frac{\partial\tilde{\boldsymbol{E}}}{\partial\boldsymbol{Q}}\right|d\boldsymbol{Q}\end{aligned} \tag{7}$$

where

$$\bar{E}\left(Q, dS_{i+\frac{1}{2},j,k}\right) = \left(i \cdot dS_{i+\frac{1}{2},j,k}\right)E + \left(j \cdot dS_{i+\frac{1}{2},j,k}\right)F + \left(k \cdot dS_{i+\frac{1}{2},j,k}\right)G \quad (8)$$

The integral in Eq. (7) is carried out along a path piecewise parallel to the eigenvectors of the Jacobian. The order in which the three eigenvalues are associated with the three subpaths linking the two states Q^+ and Q^- can substantially vary the cost for the approximate Riemann solver. The P-variant ordering has been used in the present evaluation of the integral in Eq. (7). In this way, only one flux evaluation of Eq. (8) is actually required for each of the interface fluxes at most of the cell interfaces (i.e., either subsonic or supersonic points except shock points), whereas Osher's original ordering of the subpaths in the integral requires three flux evaluations for the subsonic points. In three-dimensional problems, there are three such interface fluxes (even for supersonic flows, two of these could be subsonic) to be calculated for each cell. Thus, the saving in computation is significant.

The definition of the states Q^- and Q^+ on either side of the interface determines the order of accuracy of the scheme. If they are chosen as Q_i and Q_{i+1}, the numerical scheme for the convective terms will be only first-order accurate, which is unsatisfactory for most of the practical applications. The order of the accuracy can be improved in a very simple way by a more accurate interpolation for the states Q^- and Q^+, i.e., the κ scheme. In the present computation, $\kappa = \frac{1}{3}$ and the accuracy for discretization of the convective terms is third order. A limiter is used to avoid oscillations near the discontinuities in the solution.

The discretization scheme presented here has been investigated extensively for high-speed flow interaction problems by Qin et al.[5] It has been found to be capable of capturing both shock waves and shear layers accurately in Navier–Stokes solutions and ideal for Navier–Stokes solutions of complicated flow problems. In such an approach, no artificial viscosity is required in capturing an oscillation-free shock wave. The advantage of this type of upwind scheme over the conventional central-differencing schemes is obvious. It is preferred to the more popular Roe's approximate Riemann solver for two major reasons: First, it will not generate nonphysical expansion shocks, which can occur if Roe's scheme is used, and it requires an entropy fix. Second, the Osher operator is continuously differentiable, which provides a scope for smooth and fast convergence of the solution. On the other hand, for jet interaction problems, some investigators have favored Roe's flux differencing scheme because of its convenient extension to hot jets with thermochemistry modeling. Recently, although less straightforward than Roe's scheme, a scheme extending Osher's approximate Riemann solver to gases with an arbitrary equation of state[11] paved the way for the current approach to include thermochemistry for hot jets while maintaining the advantages of Osher's scheme.

Time Integration

We are solving steady-state problems using a time-dependent approach, i.e., we solve Eq. (1) to get the solution for Eq. (2). As the solution converges, the time-dependent term in Eq. (6) disappears and a steady-state solution is obtained. Because of computer memory limitations an explicit method was chosen that inevitably put an upper limit on the time step to satisfy the stability condition. For a steady-state solution, a local time stepping has been used for a faster convergence of the solution.

Boundary Conditions Away from the Jet

The boundary conditions are specified as follows: At the solid wall of the body, the no-slip condition is applied, i.e., all three Cartesian velocity components u, v, w are set to zero. The wall temperature is specified for the isothermal case. The pressure gradient normal to the wall is set to zero. At the outer boundary, the incoming flow properties are enforced, assuming that the body bow shock, the jet bow shock, and their interaction shock are all within the solution domain. The states on the downstream plane are extrapolated from inside the solution domain in the streamwise direction. At the two symmetry planes for a half model, the symmetrical boundary conditions are employed. Last, at the singularity line of the grid system ahead of the nose, the average of the values on the upper and lower symmetry planes are used. After the above boundary conditions have been defined, the boundary fluxes required in Eq. (6) at the solution domain boundaries then can be calculated.

Jet Boundary Condition

As the lateral jet is issued from a nozzle inside the body, a nozzle problem has to be solved to get an accurate account of the nozzle exit condition, i.e., the jet boundary condition for the flow around the body. In previous attempts, uniform flow conditions were specified using an estimated average condition at the nozzle exit. Furthermore, some investigators have used a rectangular shape for its simplicity in the computational treatment of the boundary condition so that the real nozzle exit shapes were not simulated. In doing so, they tried to match the mass flow rate at the nozzle exit. Although the assumption will not make much difference in the reaction thrust, it will certainly make a significant difference in the local flow interaction.

We believe that both the nozzle exit shape and the variation of flow properties at the nozzle exit play important roles in the flowfield interaction. In the present study, the nozzle exit shape is analytically calculated from the intersection of the nozzle and the body geometry, which is then approximated using hexahedral finite volume cell faces.

Isentropic Solution of the Nozzle Problem

To get the distribution of flow properties at the nozzle exit, we assume a one-dimensional isentropic flow inside the nozzle and that the flow directions at the nozzle exit are conical following the nozzle-wall conical geometry. This simple account of the nozzle exit flow variation is used instead of the full Navier–Stokes solution inside the nozzle because of its efficiency and reasonable accuracy for the internal nozzle flow problem, where multidimensional and viscous effects are small.

Assume that the nozzle throat area is denoted as A^* and the area of the cross section normal to the nozzle axis corresponding to a nozzle exit point is denoted as A. Using the isentropic relation between the area ratio and the Mach number, we can find the Mach number at the nozzle exit point by solving the nonlinear equation

$$\frac{A}{A^*} = \frac{1}{M}\left[\frac{2}{\gamma+1}\left(1 + \frac{\gamma-1}{2}M^2\right)\right]^{(\gamma+1)/2(\gamma-1)} \quad (9)$$

for M. To solve Eq. (9), we used the Newton iterative method for the nonlinear equation

$$g(M) = \left[\frac{2}{\gamma+1}\left(1 + \frac{\gamma-1}{2}M^2\right)\right]^{(\gamma+1)/2(\gamma-1)} - \frac{A}{A^*}M = 0 \quad (10)$$

We can easily get

$$g'(M) = M\left[\frac{2}{\gamma+1}\left(1 + \frac{\gamma-1}{2}M^2\right)\right]^{(3-\gamma)/2(\gamma-1)} - \frac{A}{A^*} \quad (11)$$

Given an initial guess for the jet-exit Mach number at the point, say, M_0, the Newton iterative method can be written as

$$M_{n+1} = M_n - \frac{g(M_n)}{g'(M_n)}, \qquad \text{for } n = 1, 2, \ldots \quad (12)$$

This solution for the Mach number is carried out for each point at the nozzle exit because the area ratio can be different from point to point.

The pressure and temperature then can be found from

$$p_t/p = \{1 + [(\gamma-1)/2]M^2\}^{\gamma/(\gamma-1)} \quad (13)$$

$$T_t/T = 1 + [(\gamma-1)/2]M^2 \quad (14)$$

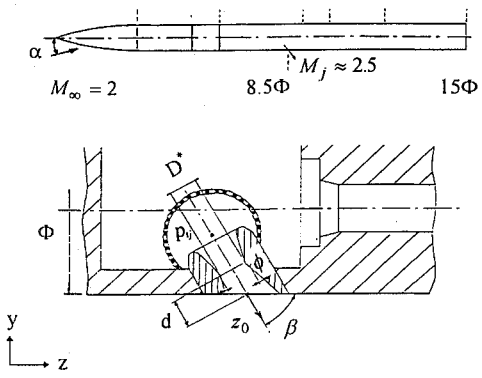

Fig. 1 ONERA model of ogive-cylinder body and jet nozzle details.

Calculation of A/A^*

The solution of the Mach number from Eqs. (9–12) requires the area ratio at the jet exit point. Consider a nozzle issuing at an angle of β to the body axis (refer to Fig. 1 for the notation). The area ratio can be calculated as

$$\frac{A}{A^*} = \frac{\left\{D^* + 2[d + (z - z_0)\cos\beta]\tan\phi\right\}^2}{D^{*2}} \tag{15}$$

Velocity Directions at Nozzle Exit

We can easily find the velocity magnitude from the Mach number and the temperature. To determine the velocity direction, we assume a conical flow at the nozzle exit, which can be calculated from the geometric data of the conical-shaped nozzle.

Results

Wind-Tunnel Test Cases

Because of the availability of the well-documented set of ONERA data, the capability of the present development for numerical simulation of supersonic lateral jets has been tested under their wind-tunnel test conditions. The geometry is a finless ogive-nosed circular body with a cold jet issuing transversely from the cylindrical body. Figure 1 shows the general arrangement and details of the jet nozzle. The wind-tunnel tests were carried out under the following conditions.

Income flow conditions:

$$M_\infty = 2.0, \qquad Re_\infty = 1.36 \times 10^7/\text{m}, \qquad T_\infty = 166\ \text{K},$$
$$T_{t\infty} = 299\ \text{K}, \qquad p_{t\infty} = 1.1 \times 10^5\ \text{N/m}^2$$

Incidence:

$$\alpha = -10, 0, 10, 20\ \text{deg}$$

Jet stagnation conditions:

$$p_{tj}/p_\infty = 110, \quad \text{i.e.,} \quad p_{tj}/p_{t\infty} = 14$$

or

$$p_{tj}/p_\infty = 220, \quad \text{i.e.,} \quad p_{tj}/p_{t\infty} = 28$$
$$T_{tj} = 299\ \text{K}$$

Given the jet stagnation conditions, the jet conditions can be calculated using the method presented earlier. Five cases have been run with various jet stagnation conditions and incidences as listed in Table 1.

Table 1 Test cases

Case no.	I	II	III	IV	V
$p_{tj}/p_{t\infty}$	14	28	28	28	14
α, deg	0	0	5	10	20

Computational Grid Generation

A three-dimensional algebraic grid-generation technique has been used to generate the body-fitted grid around the geometry. It uses the transfinite interpolation technique for a structured single-block grid. The flexibility in tuning the normality and clustering near the wall made it suitable for Navier–Stokes simulations. The grid is clustered in the nozzle exit area in the wall-surface-grid generation to resolve the geometry of the nozzle exit and the severe gradients of the flow properties around it. The outer-surface grid is generated to include in the computational domain the body bow shock waves depending on the angle of attack. The three-dimensional field grid is then generated from the surface grids using the defect Hermite interpolation. The grid is required to be normal and clustered in the normal direction at the wall, which is controlled by two parameters in the grid generator. Several grids were generated for the five cases because of variation in the angle of attack. The grid size is fixed for all cases, with 97 in the streamwise direction, 65 in the circumferential direction, and 65 from the wall to the outer boundary, which has exhausted the memory resources on the workstation. All computations were run in double precision.

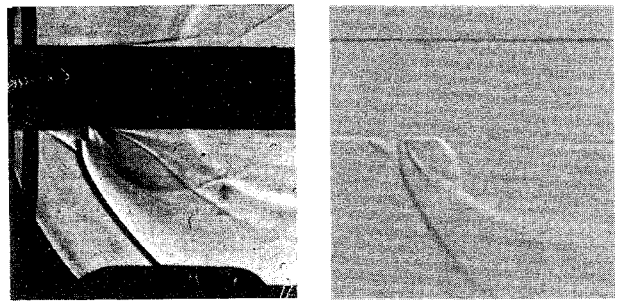

Fig. 2 Comparison of experimental schlieren picture (left) and computational density gradient (right) (case I).

Ideally, a grid sensitivity study should be carried out for each case to investigate how strongly the numerical solution depends on the grid density and whether the solution obtained is grid-converged. Unfortunately, in the present cases we found it is difficult to carry out such a study for the three-dimensional problem. A reasonable grid refinement in all three directions results in a much larger three-dimensional problem that the workstation could not handle because of the much larger memory requirement. However, confidence on the accuracy of the approximate-Riemann-solver-based numerical discretization scheme has been established by many investigators, including our previous research in this area. Qin et al.[5,12] demonstrated that the results produced by Osher's scheme have much less contaminating numerical diffusion compared with other schemes incorporating less physics in the flux formulation and therefore are much less sensitive to the grid density.

Computational Results and Discussion

The computations were carried out on a SGI Indigo2 workstation with 96 Mb of RAM. It took 63 CPU seconds per iteration, i.e., 1.6×10^{-4} CPU second per cell point per iteration. A typical run took about 5000 iterations for a L_2 norm reduction of the residuals of 2.5 orders, which took about 87.5 CPU hours to run on the workstation.

Computations have been carried out for the five test cases listed in Table 1. The effect of jet stagnation pressure on the penetration distance of the jet stream is observed and the angle of attack reduces the distance of the upstream influence of the jet shock/boundary-layer interaction. All cases exhibit similar local interaction structure around the jet exit, whereas the downstream interaction can be quite different depending on the angle of attack and the jet stagnation pressure.

Figure 2 compares the general features of the flow near the jet for case I. Good agreement on the flow structure near the jet exit is observed between the schlieren picture from the wind-tunnel test and the density gradients on the symmetric plane from the computation. The strong shock wave in front of the lateral jet can be seen clearly in both pictures and the λ shock at the foot of the bow shock is well captured by the computation. Note that the experimental schlieren picture reflects the density gradient normal to the knife edge across the three-dimensional field, whereas the density gradient on the

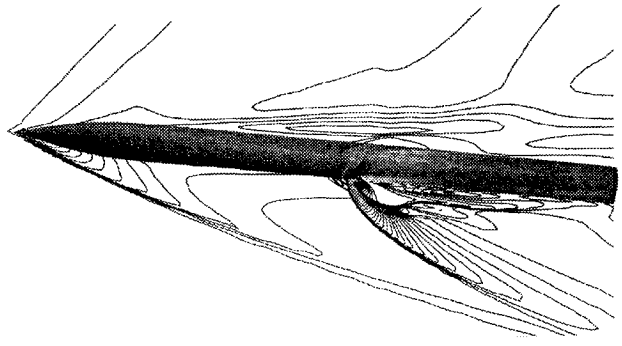

Fig. 3 Pressure contours on the symmetrical planes (case V).

a) $z/\Phi = 10$ b) $z/\Phi = 12$ c) $z/\Phi = 15$

Fig. 4 Comparison of total pressure contours.

symmetric plane shown on the left may have missed some flow features off the plane, which explains the difference downstream of the jet exit.

Because of the relatively more complicated flow features at high angles of attack, case V is presented and discussed in more detail. Figure 3 plots the pressure contours on the symmetrical planes and the pressure shade on the body surface. Observed from the plots are the bow shock wave around the body, and the bow shock wave in front of the jet stream, which extends to the leeward side. Also observed is the λ-shock structure at the foot of the jet bow shock wave, which introduces two major high-pressure zones ahead of the jet exit on the body surface.

In Fig. 4, the total pressure contours from the wind tunnel data and the computation are compared for three cross-sectional planes. They are at 10, 12, and 15 caliber from the nose, which corresponds to 1.5, 3.5, and 6.5 caliber, respectively, downstream of the center of the jet exit. Because the three-dimensional grid surfaces, except the rear surface, generated for the computation are not straight cuts normal to the body axis as in the wind-tunnel data, the computational results have been interpolated to the experimental points to make the comparison for cross sections at 10 and 12 caliber. The primary features of the vortical flow structures compare reasonably well, including the primary vortex on the leeward side, the jet core, and the vortical flows around the jet. The multiple vortical structure can be seen best at the 12-caliber cross section. On the leeward side, the primary and the secondary vortical flows can be seen. On the windward side (jet-issuing side), the jet core, the vortical flows around the jet, and the vortical flow between the jet core and the body surface are observed. (Some noises on the side of the body in the experimental data may be attributable to the experimental uncertainties.) Although the positions of these flow structures are in reasonably good agreement at these cross sections, discrepancies exist in the flow structure around the jet at the 10-caliber cross section. A similar multiple vortical structure has been established in the experimental data but the computational results did not show these structures around the jet core. For this high-angle-of-attack case, both computation and the experiment show that the jet core has been diffused at the rear surface (15 caliber) and the primary vortex generated by the jet wraps around the side of the body.

The global vortex flow structure can be seen from the streamline plot in Fig. 5. The primary and secondary vortices on the leeward side are disturbed by the horseshoe vortex, which results in an enhanced secondary vortical feature downstream and pushes the primary vortex farther away from the body. On the windward side, the vortex around the jet stream is obvious. A relatively weak vortical flow also can be observed in the streamlines between the main vortex and the body downstream of the jet exit.

The global vortical flow system is confirmed in the surface-skin-friction line plots, which show the trace of the vortical flow on the body surface. Generally, the convergent skin-friction lines indicate flow separation, whereas the divergent skin-friction lines indicate reattachment. In Fig. 6, the view is slightly upward so that a better picture for the lower side of the body can be seen. The horseshoe vortex develops into a complicated vortical flow system influencing the flow on the leeward side of the body. Also observed are the separation lines behind the jet exit. In Fig. 7, the surface skin-friction lines are viewed downward for a better observation of the leeward side of the body. The primary and secondary separation lines are clearly seen ahead of the jet-interference region. Both of these separation lines are strongly distorted by the horseshoe vortex system because of jet interaction.

Pitot pressure contours on a number of computational crossflow surfaces are plotted in Fig. 8 to examine both the field vortical system and the internal shocks, which are not shown in the total pressure plots in Fig. 4. For a section before the jet interaction region (Fig. 8a), we can see the body bow shock, the primary and secondary vortices on the leeward side, and a weak shock on the side of the body attributable to the vortical flow. In Fig. 8b, which cuts the jet exit, the high-pressure jet, the jet shock, and the horseshoe vortex

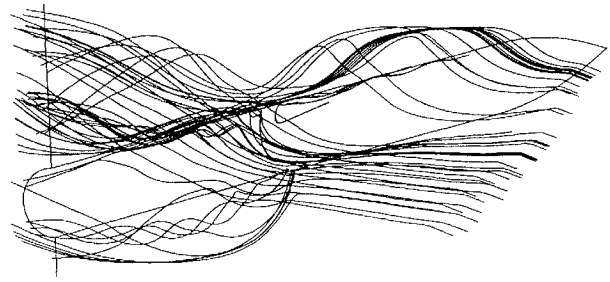

Fig. 5 Streamlines around the body.

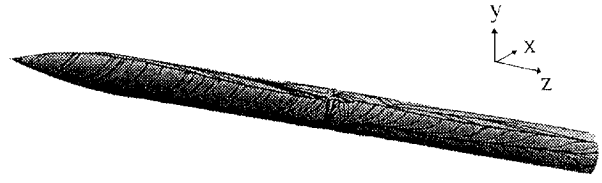

a) Global view

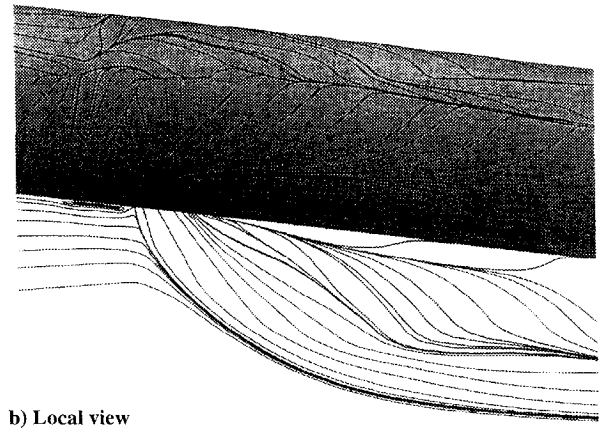

b) Local view

Fig. 6 Skin-friction lines on the body surface, upward-side view (including surface streamlines on the symmetrical surface).

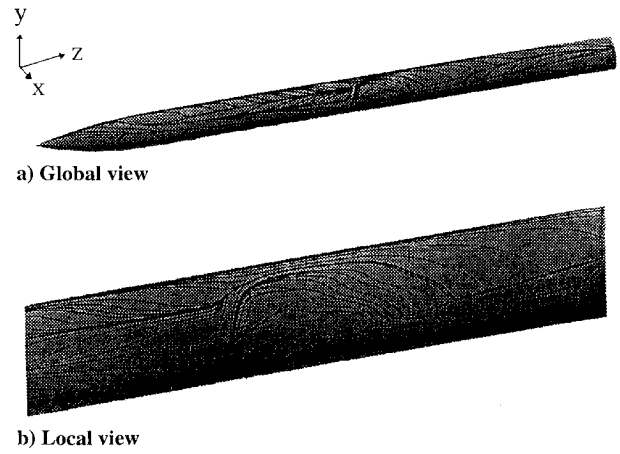

a) Global view

b) Local view

Fig. 7 Skin-friction lines on the body surface, downward-side view.

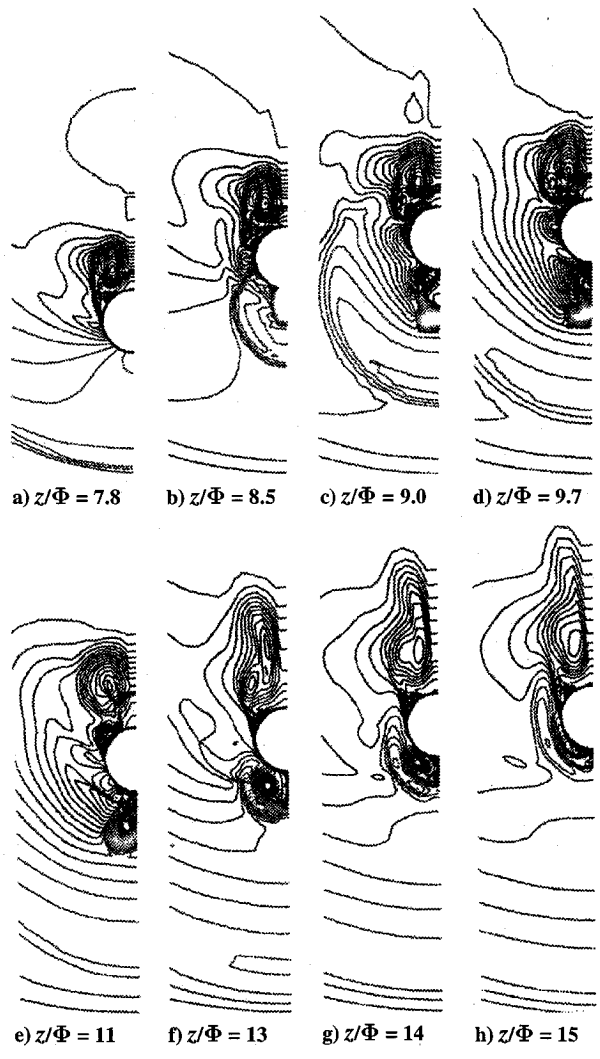

Fig. 8 Pitot pressure contours at computational crossflow surfaces.

at the foot of the shock can be observed. The jet shock expands downstream, interacts with the vortical system on the leeward side, and eventually merges with the body shock on the windward side (Figs. 8c–8f). The recompression shock downstream of the jet exit can be observed clearly in Figs. 8d–8f somewhere between the jet stream and the body surface. Also observed is the weak embedded shock beside the vortical system on the leeward side (Fig. 8e).

Conclusions

An isentropic jet-boundary condition has been developed to account for the variation of the flow properties at the jet exit. The geometry of the jet exit is matched in the computation through the intersection of the jet nozzle and the body surface. The numerical simulation using a high-resolution scheme has been carried out for the ONERA test cases at various angles of attack and jet pressure ratios involving a strong supersonic lateral jet in a supersonic crossflow. Major features of the flowfield are captured including the bow shock wave generated by the jet and its interaction with the boundary layer, the λ-shock at the foot of the bow shock wave and the induced horseshoe vortex, a pair of vortices generated around the main jet stream downstream, a pair of weak vortices at the back of the jet exit, and the recompression shock downstream of the jet exit. The primary and secondary body vortices over the leeward side and their interaction with the jet shock and the horseshoe vortex also are captured for the higher-angle-of-attack cases. Comparison of the computed vortical system downstream of the jet exit with the experimental data through total pressure contours gives reasonable agreement.

Acknowledgments

The authors acknowledge the financial support from the Defence Research Agency (DRA) and the United Kingdom Ministry of Defence for the research. They wish to thank M. P. Champigny and ONERA for permission to include their experimental data in this paper. They also would like to thank Trevor Birch of DRA for helpful discussions.

References

[1]Shang, J. S., McMaster, D. L., Scaggs, N., and Buck, M., "Interaction of Jet in Hypersonic Cross Stream," *AIAA Journal*, Vol. 27, No. 3, 1989, pp. 323–329.

[2]Rizzetta, D. P., "Numerical Simulation of Slot Injection into a Turbulent Supersonic Stream," *AIAA Journal*, Vol. 30, No. 10, 1992, pp. 2434–2439.

[3]Dash, S. M., York, B. J., Sinha, N., Lee, R. A., Hosangadi, A., and Kenzakowski, D. C., "Recent Development in the Simulation of Steady and Transient Transverse Jet Interactions for Missile, Rotorcraft, and Propulsive Applications," *Computational and Experimental Assessment of Jets in Cross Flow*, CP-534, AGARD, 1993 (Paper 29).

[4]Qin, N., and Richards, B. E., "Finite Volume 3DNS and PNS Solutions of Hypersonic Viscous Flow Round a Delta Wing Using Osher's Flux Difference Splitting," *Proceedings of the Workshop on Hypersonic Flows for Reentry Problems*, edited by J. A. Desideri, R. Glowinski, and J. Periaux, Vol. 2, Springer–Verlag, Berlin, 1992, pp. 947–959.

[5]Qin, N., Scriba, K. W., and Richards, B. E., "Shock-Shock, Shock-Vortex Interaction and Aerodynamic Heating in Hypersonic Corner Flow," *Aeronautical Journal*, Vol. 95, No. 945, 1991, pp. 152–160.

[6]Clark, S. W., and Chan, S. C., "Effects of Turbulence Models and Adaptive Grids on the Jet Interaction Flowfield," AIAA Paper 93-3524, Aug. 1993.

[7]Dhinagaran, R., and Bose, T. K., "Two-Dimensional Jet Interaction Flowfield Predictions with an Algebraic Turbulence Model," AIAA Paper 95-2242, June 1995.

[8]Baldwin, B. S., and Lomax, H., "Thin-Layer Approximation and Algebraic Turbulence Model for Separated Turbulent Flows," AIAA Paper 78-257, Jan. 1978.

[9]Degani, D., and Schiff, L. B., "Computation of Turbulent Supersonic Flows Around Pointed Bodies Having Cross Flow Separation," *Journal of Computational Physics*, Vol. 66, No. 1, 1986, pp. 173–196.

[10]Birch, T. J., Qin, N., and Jin, X., "Computation of Supersonic Viscous Flows Around a Slender Body at Incidence," AIAA Paper 94-1938, June 1994.

[11]Suresh, A., and Liou, M. S., "Osher's Scheme for Real Gases," *AIAA Journal*, Vol. 29, No. 6, 1991, pp. 920–926.

[12]Qin, N., "A Comparative Study of Two Upwind Schemes as Applied to Navier–Stokes Solutions for Resolving Boundary Layers in Hypersonic Viscous Flow," Dept. of Aerospace Science, G.U. Aero Rept. 9120, Univ. of Glasgow, Scotland, UK, 1991.

R. M. Cummings
Associate Editor